Scalable Elasticoluminescent Strain Sensor for Precise Dynamic Stress Imaging and Onsite Infrastructure Diagnosis

Linsheng Liu, Chao-Nan Xu,* Akihito Yoshida, Dong Tu, Naohiro Ueno, and Shigenobu Kainuma

Precise dynamic stress/strain imaging is critical for a broad range of research and engineering analyses ranging from micrometer to meter-scales, but there is no precise multiscale strain sensor, especially for onsite real-time structural health monitoring. Here, a scalable elasticoluminescent strain sensor is presented for solving worldwide structural diagnosis problems ranging from micrometer to meter-scales. Significant progress has recently been made on both highly sensitive elasticoluminescent sensors and quantitative evaluations in dynamic stress/strain imaging. The precise dynamic imaging of stress/strain and onsite fracture inspection and danger-level (stress concentration) diagnoses on large-scale infrastructures are demonstrated. The innovative scalable strain sensor would prospectively open a new era in multiscale strain imaging research and contribute to multifield research related precise dynamic stress/strain imaging and healthcare of structures.

1. Introduction

After the sudden collapse of I-35W Mississippi River Bridge (Bridge 9340, USA) in 2007 and the burst of a stream pipe in midtown Manhattan (also in 2007) that both due to stress concentration at the structure and lack of effective maintenance of fatigue microcracks, developing efficient techniques for dynamic and precise stress/strain imaging on large-scale

Dr. L. S. Liu, Prof. C.-N. Xu, Dr. A. Yoshida, Dr. D. Tu
Advanced Manufacturing Research Institute
National Institute of Advanced Industrial Science and Technology (AIST)
Shuku-machi 807-1, Saga 841-0052, Japan
E-mail: cn-xu@aist.go.jp

Prof. C.-N. Xu
Department of Molecular and Material Sciences
Kyushu University
Fukuoka 816-8580, Japan

Prof. N. Ueno
Graduate School of Science and Engineering
Saga University
Saga 840-8502, Japan

Prof. S. Kainuma
Department of Civil Engineering
Kyushu University
Fukuoka 819-0395, Japan

The ORCID identification number(s) for the author(s) of this article can be found under https://doi.org/10.1002/admt.201800336.

structures attracted world-wide attention in order to ensure effective maintenance and avoid recurrence of such severe disasters.[1–3] In December 2017, a serious incident happened at a Shinkansen bullet train of Japan due to anomalous load caused fatigue cracks and rupture in an undercarriage,[4] and this sudden incident further enhanced the urgent necessity to predict the fracture (damage) of infrastructures. Since conventional magnetic particle testing (MT), penetrant testing (PT), and ultrasonic testing (UT) methods are difficult for precise large-scale infrastructure diagnosis, many techniques were proposed on this topic in recent years, such as sensing techniques of electrical resistance or capacitive MEMS strain sensors and piezoelectric sensors were proposed for precise strain or anomaly detection, but these methods still had limitations for strain imaging on real world structures due to the sensor scale and/or spatial resolution.[5–8] On the other hand, new types of sensors based on photoelectric methods such as assembled nanowires/nanotubes or microstructured rubber layers,[9–15] stretchable and flexible strain sensor with conductive nanostructure for sensitive detection of human motion,[16] piezotronic/piezo-phototronic-effect enhanced light emitting smart sensors,[17,18] and flexible or bionic mechanosensors were proposed as effective sensing techniques for dynamic imaging of pressure or stress and diagnosing movement disorders in high-resolution.[19–23] However, fabrication methods of the abovementioned nanowire array or flexible smart sensors are complicated, and they are inconvenient for scalable precise stress/strain imaging and especially difficult for large-scale application and onsite real world infrastructures.

Herein, we report another mechanism of largely scalable and flexible strain sensor using elasticoluminescent smart paint for challenge to solve worldwide structural diagnosis problems ranging from micro to macroscales. The elasticoluminescence presented in this study also called elastico-mechanoluminescence is a unique form of mechanoluminescence (ML) that can generate repeatable and reproducible light emission during elastic deformation.[24–29] The new scalable elasticoluminescent strain sensor has great significance on high sensitivity and precise dynamic stress/strain imaging, and onsite fracture inspection and diagnoses on large-scale infrastructures. The innovative scalable strain sensor would prospectively open a

**ADVANCED
SCIENCE NEWS**
www.advancedsciencenews.com

**ADVANCED
MATERIALS
TECHNOLOGIES**
www.advmattechnol.de

new era in multiscale strain imaging research and contribute to precise dynamic stress/strain imaging related multifield researches ranging from material science, physics, chemical, to biology and structure engineering.

2. Scalable Elasticoluminescent Strain Sensor

2.1. Brief Review

The novel ML material of Eu-doped $SrAl_2O_4$ (SAOE) was first innovated by highly controlling of the defect in crystal structure, and the concept on dynamic stress/strain imaging utilizing such a new ML was pioneered by Xu group.[25–28] Thereafter, many researchers started researches on SAOE, and SAOE was developed for dynamic stress/strain imaging from micrometer to meter scales, both experimental analyses and theoretical simulation.[1,30–40] The grain sizes of SAOE were fabricated to submicron/micron grain by solid phase method and 10–20 nm single-crystal by a unique two-liquid ultrasonic spray-pyrolysis method,[41,42] and the detailed crystal structure was clarified by synchrotron X-ray powder diffraction analysis.[43] Images of the ML material and the scalable sensors for dynamic strain/stress imaging are shown in **Figure 1**. a) shows a typical crystal structure of monoclinic α-SAOE;[43] b) shows a 10 nm single-crystal ML particle releasing ML based light emission during repeated loading,[41,42] and this can potentially enable strain imaging of microscale objects with submicron or micrometer sizes; c) shows the in situ transmission electron microscope (TEM) observation of elastic deformation of α-SAOE within the domain boundary during a repetitive loading by nanoindenter movement;[44] d) shows the photograph and the enlarged scanning electron microscope (SEM) image of ML particles that have an averaged grain size of about 1 μm; e) shows the photograph of scalable elasticoluminescent strain sensor of ML paint film on a metal substrate and the enlarged SEM image showing both the ML particle distribution within the ML paint and the strongly adhesive interface between the paint and substrate, in which the scalable sensor is continuously networked; f) is a ball coated with ML paint and the ML image generated by finger pressure; g) shows kinetic biomechanical ML imaging (using a simulated femur viewed from the posterior side)[32] generated by applying to the femoral head a load of 0.1–1.9 kN, and this enables potential dynamic stress/strain imaging for biological or robotic applications.

ML paint consists of microparticles and adhesive resin, and after forming the paint film, it works in whole as scalable sensors from micrometer to meter scales. The scalable elasticoluminescent strain sensor (as shown in Figure 1e–g) can actively emits light in response to the local stress in real-time (with a response time ≤ 50 μs)[45] during loading. Contrary to the reported pressure imaging smart sensors based on nanowire arrays
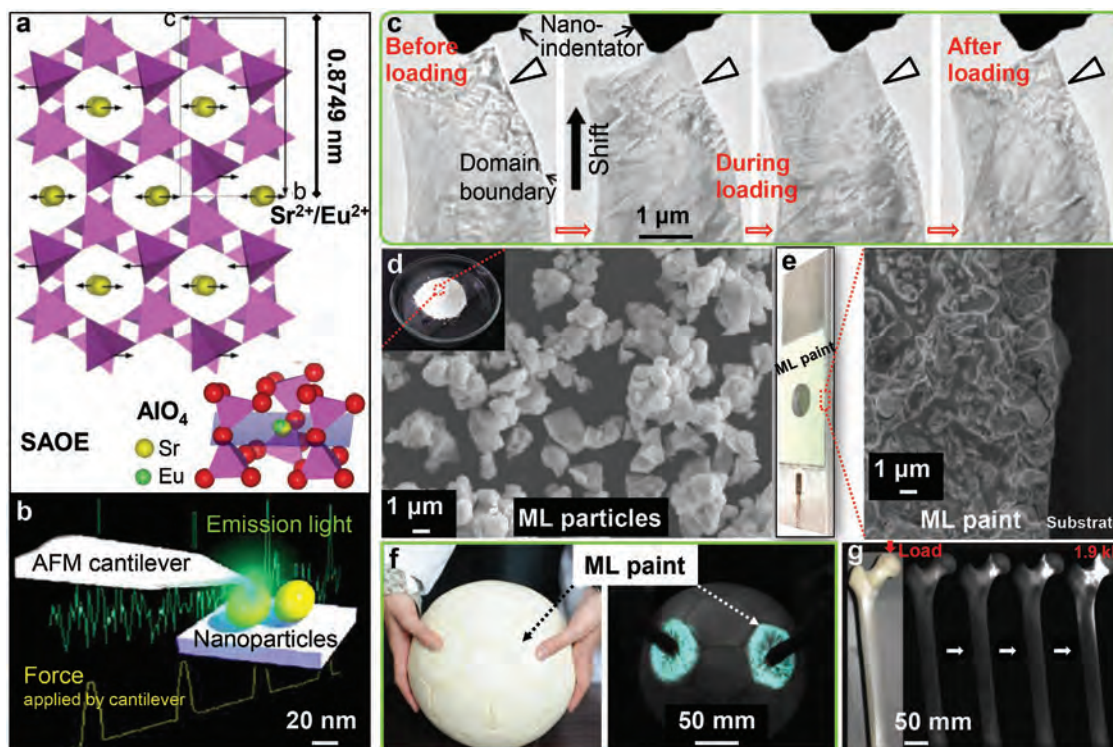
Figure 1. ML material and its multifield scalable application for dynamic strain/stress imaging. a) A typical crystal structure of monoclinic α-SAOE. Reproduced with permission.[43] Copyright 2017, AIP Publishing. b) A 10 nm single-crystal ML particle releasing ML based light emission during repeated loading.[41] c) In situ TEM observation of elastic deformation in α-SAOE under nanoindentation (loading), in which the vertical black arrow shows the shift direction of the sample and the white arrow-head at each upper-right corner indicates an area where the twin interfaces disappear during loading. Reproduced with permission.[44] Copyright 2013, Elsevier. d) SEM image of SAOE ML particles. e) SEM image of the scalable elasticoluminescent strain sensor of ML paint on a metal substrate containing the strongly adhesive interface between the ML paint and substrate. f) A ball coated with the ML paint and the ML generated by finger pressure. Reproduced with permission.[35] Copyright 2017, Fuji Technology Press Ltd. g) Kinetic biomechanical ML imaging generated by applying a load of 0.1–1.9 kN to the femoral head using a simulated femur.[32]

**ADVANCED
SCIENCE NEWS**

www.advancedsciencenews.com

**ADVANCED
MATERIALS
TECHNOLOGIES**

www.advmattechnol.de

that the spatial-resolution is limited by the sensor device and has a highest resolution of 2.7 µm at a pixel density of 6350 dpi and maximum scale of 8.0 mm (when oriented at high-resolution pressure imaging)[17] and a resolution of 254 µm at 100 dpi and maximum scale of 25.4 mm (when oriented at full dynamic-range pressure imaging),[18] the present new scalable sensor is continuously networked as the ML particles are multilayer overlapped and the sensor has a resolution much higher than 1 µm; consequently, the resolution only depends on the imaging (observation) system. The ML of other material, such as ZnS:Mn, was also investigated for dynamic 2D pressure mapping but not for the multiscale application, applicable map ranging from 0.6 to 50 MPa or 2.2 to 40.6 MPa were achieved for the designed specific devices.[46,47] The scalable strain sensor reported here is sensitive and greatly significant for multiscale applications ranging from micrometer to meter-scales, and the high-precision in strain/stress imaging is quantitatively evaluated.

2.2. Quantitative Strain Evaluation

To quantitatively evaluate the relationships between the ML values of the scalable elasticoluminescent strain sensor of ML paint and the absolute strains measured by the high-precision strain gauge, experiment was carried out and shown in **Figure 2**. Figure 2a shows the schematic diagram of experimental setup for the ML measurement system and a material testing system (MTS).

Figure 2b shows the ML values detected by the charge-coupled device (CCD) camera in comparison to the synchronous absolute strains at a range of 0–2000 µST for two types of scalable elasticoluminescent strain sensors. Type 1 sensor is well applicable for imaging of strains ≥ 600 µST when detected by a commercial CCD camera,[1] while Type 2 sensor is made from the newly developed ultrasensitive SAOE material that is firstly reported here and well applicable for imaging of lower strains and has significant ML enhancement than Type 1 at strains ≤ 1000 µST. Type 2 sensor has an unprecedented threshold-less sensitivity to detect micron strains when detected by the photon counting system and still has a notable monotonic relationship with smaller strains of 1–200 µST as shown in Figure 2c. While Figure 2b shows that the ML values of Type 2 sensor increases monotonically with increasing strain at a strain ≤ 1800 µST, and it means that Type 2 sensor is much more sensitive for evaluating small strains. Figure 2c shows that although Type 1 SAOE has a threshold of about 100 µST for strain/stress sensing, Type 2 sensor has no threshold for strain/stress sensing and still has strain sensitivity at the lowest micron-strain range, and its ML intensity has a monotonic relationship with small strain and exhibits a sensitive response to the strain.

For the paint film sensor, the elastic module is ≈ 1 GPa, and according to Hooke's law, a strain sensitivity of 1 µST is equivalent to a stress sensitivity of 1 kPa and it means that this paint film would be suitable as an excellent microforce sensor for piconewton-scale precision tests (at a 1×1 µm area). This would greatly improve the dynamic range and accuracy of ML detection, particularly beneficial to the development of

bioimaging with single-cell resolution, and the sensing and control in microrobotic cell manipulation.[48,49] It should be noted that all the measurements for quantitative evaluations are carried out under the standardized condition (i.e., the irradiation and waiting times of 60 and 300 s, respectively) explained in detail in the Experimental Section.

Recently, we have succeeded in quantitative strain evaluation in high-precision from the ML intensity and its variance rate, and the quantitatively evaluated strains are compared to the synchronously measured absolute strains and shown in Figure 2d, in which the averaged results are presented with error bars of four times of repetitions. To verify the robustness of strain evaluation independent of strain increasing rate, more detailed measurements were carried out at the same maximum strain but of different strain increasing rates of 500, 1000, and 2000 µST s^{-1} (repeated no less than two times for each strain increasing rate), and the evaluated strains with error bars are compared to the absolute ones and shown in Figure 2e (Type 1 sensor as an example). The precise evaluation results in Figure 2d,e strongly validate both the effectiveness and high-precision of the strain evaluation method and the correctness of the calibration method. Detailed information for sample preparation and quantitative evaluation are shown in the Experimental Section.

3. Precise Dynamic Strain Imaging

Based on the precise strain evaluation for the planar specimen, the precise and dynamic imaging is verified using complicated structures with complicated strains and strain variance rates. As a representative proof experiment, circle-hole specimen is demonstrated. Considerable researches have been carried out on the stress concentration caused by the existence of circular holes on a planar specimen, both theoretically and experimentally.[1] Our experiments are consistent with the reported results[1] that both the strain distribution values and strain variance rates on the circle-hole specimen differ on locations even when the increasing rate of tensile/compressive load is kept constant.

Al alloy plate (JIS A5052, size of $225 \times 25 \times 2.9$ mm) with a central hole was investigated following the schematic diagram shown in Figure 2a, and **Figure 3** shows the ML images and quantitatively evaluated strain distribution imaging in comparison to the strains obtained from both the strain gauges and the finite element method (FEM) simulated results. Figure 3a shows the bright field image of the ML paint bonded on the specimen, where the strain distribution of A to B is an important index and would be displayed. Figure 3b shows the evaluated strains along the central line (from A to B) with either Type 1 or 2 sensor in comparison to the FEM simulation results and the absolute strains (shown by star-marks) calculated as equivalent strains from the measured values by the rosette strain gauges (622 µST at 3.0 mm and 840 µST at 19.6 mm, respectively) at the load of 2.4 kN. The equivalent strains evaluated by either Type 1 or 2 sensor match well with both the FEM simulated ones and the measured ones using strain gauges, and the results are shown in comparison in Figure 3b. Figure 3c shows FEM simulation, and Figure 3d–g shows grayscale
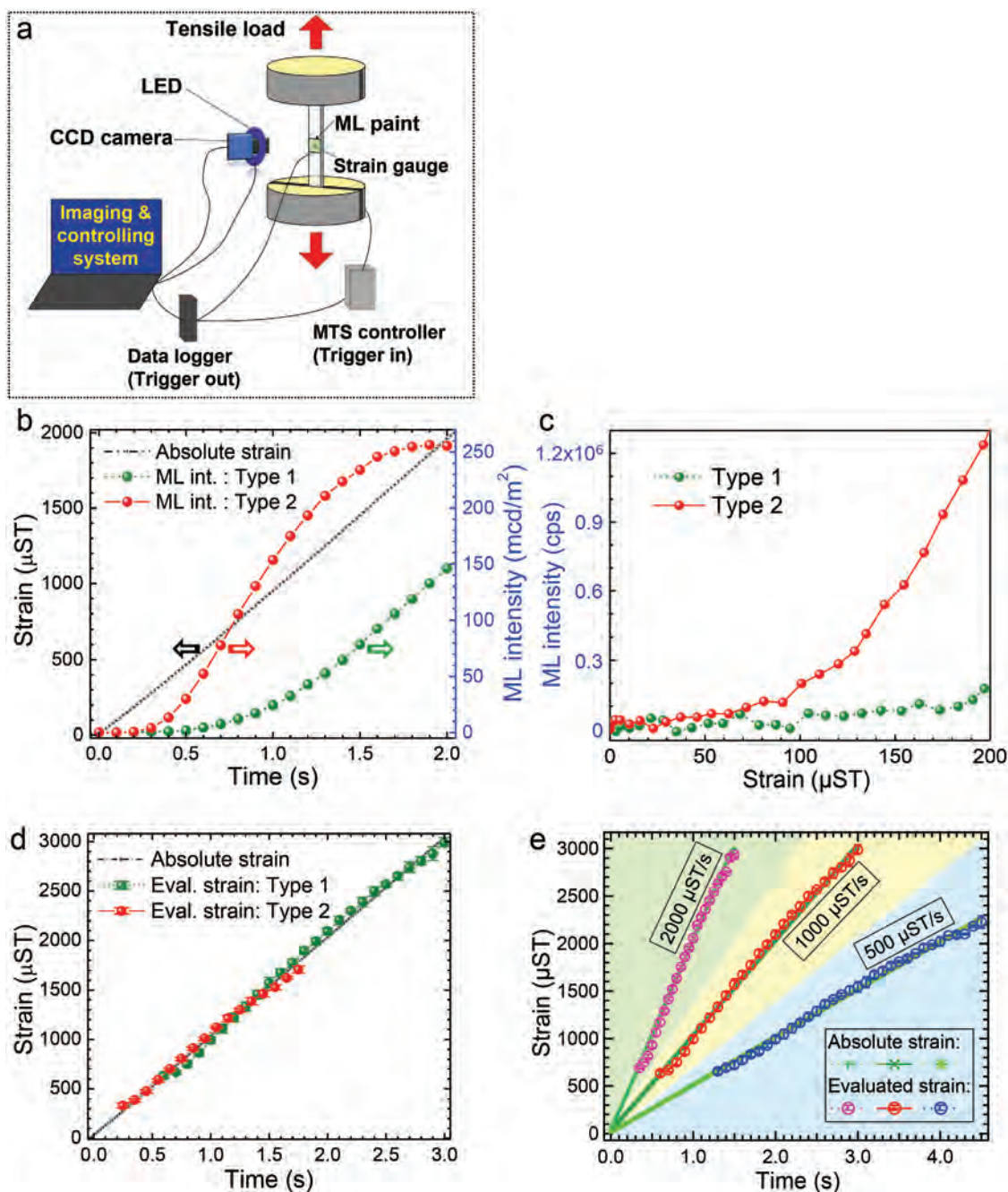
Figure 2. Schematic diagram of experimental setup for ML measurement and quantitatively evaluated strains in comparison to absolute ones. a) Schematic diagram of the ML measurement system and a material testing system (MTS). b) ML values of both Type 1 and 2 sensors detected by a CCD camera in comparison to synchronous absolute strains along with the loading time. c) ML values of both Type 1 and 2 sensors under small strains when detected by the photon counter. d) Evaluated strains for both Type 1 and 2 sensors with error bars of four times of repetitions (at a strain increasing ratio of 1000 µST s^{-1} and a maximum strain of 3000 µST). e) Evaluated strains with repetition error bars for measurement at strain increasing rates of 500, 1000, and 2000 µST s^{-1}, respectively, to confirm that the precise strain evaluation is independent of strain increasing rate (Type 1 sensor as an example).

images of ML and pseudo color ones of the evaluated strains at this load for both Type 1 and 2 sensors. Although a large difference can be found in the ML intensities shown in Figure 3d,f as the maximum ML values are set to be 4 times in difference, the evaluated strains shown in Figure 3e,g are similar except for the results along the vertical direction (i.e., γ-direction), where only Figure 3g of Type 2 sensor shows a clear distribution pattern.

A luminance of 5 mcd m^{-2} is shown as the lower limit in ML imaging since it is close to the background noise level. The significant superiority in sensitivity of Type 2 sensor is clearly shown in **Figure 4**, where the dynamic conditions under smaller maximum loads of 0.6, 1.2, and 1.8 kN (refer to Movie S1 of the Supporting Information for more detailed information). The ML intensities of Type 1 sensor are much weaker than that
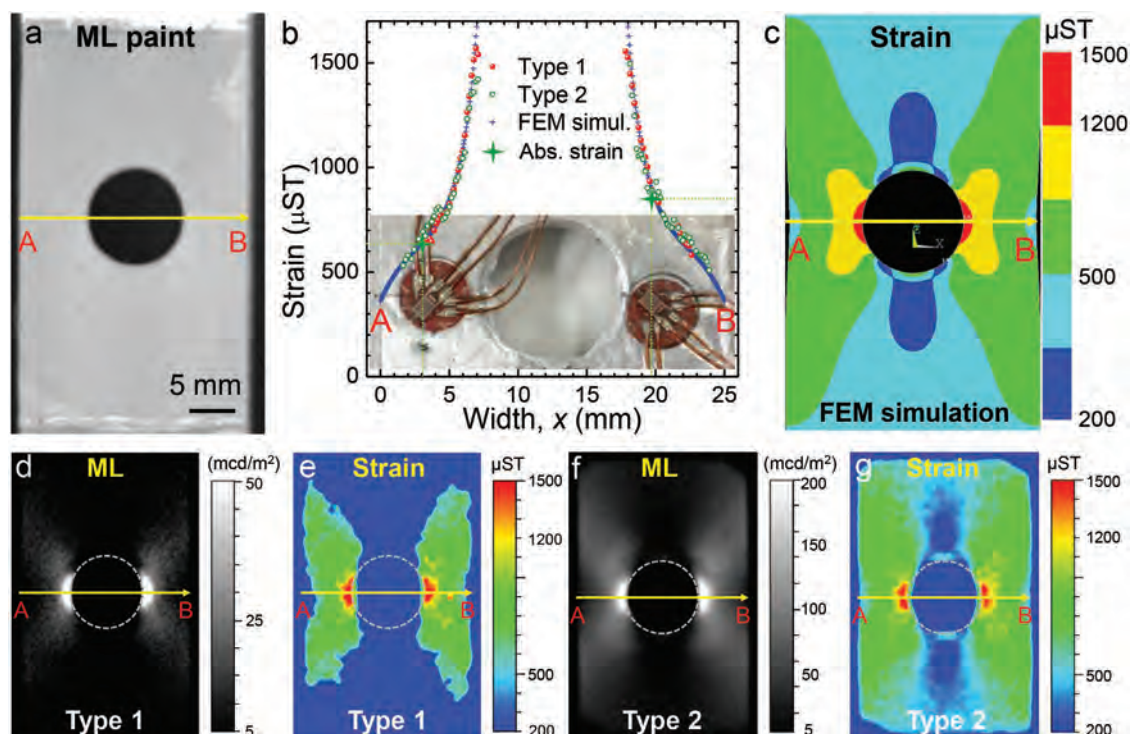
Figure 3. Quantitative strain analyses by ML, strain gauges, and FEM simulation. a) Bright-field image of ML paint around a central hole on an Al alloy plate of $225 \times 25 \times 2.9$ mm. b) Evaluated equivalent strains verified by both a pair of (3-axis) rosette strain gauges and FEM simulation. c) Image of equivalent strain distribution by FEM simulation. Images of ML d) and evaluated strain e) for Type 1 sensor, and that of ML f), and evaluated strain (g) for Type 2 sensor at load of 2.4 kN.

of Type 2, and the intensity ranges are shown in 7, 8.5, and 10 times in difference for loads of 1.8, 1.2, and 0.6 kN, respectively, for clear observation as shown in Figure 4. The significant superiority in sensitivity of Type 2 sensor can be clearly seen from both the ML and evaluated equivalent strain images. When the maximum strain becomes about 750 µST under load of 1.2 kN (1.0 s), Type 2 sensor can clearly show patterns of ML and precise strain images, while Type 1 sensor can only show these results in quite small areas where strains are higher than 600 µST; further, when the maximum strain becomes about 375 µST (0.6 kN, 0.5 s), Type 2 sensor can still show visible ML and strain images in the areas where the strains are higher than 300 µST, while Type 1 sensor was difficult to show ML image among the background noise. Even for the strain of about 1125 µST (1.8 kN, 1.5 s), Type 2 sensor can show clear ML and strain distribution patterns, while Type 1 sensor can only show results of quite limited areas. Different types of sensors can be optimized for wide range of strain imaging.
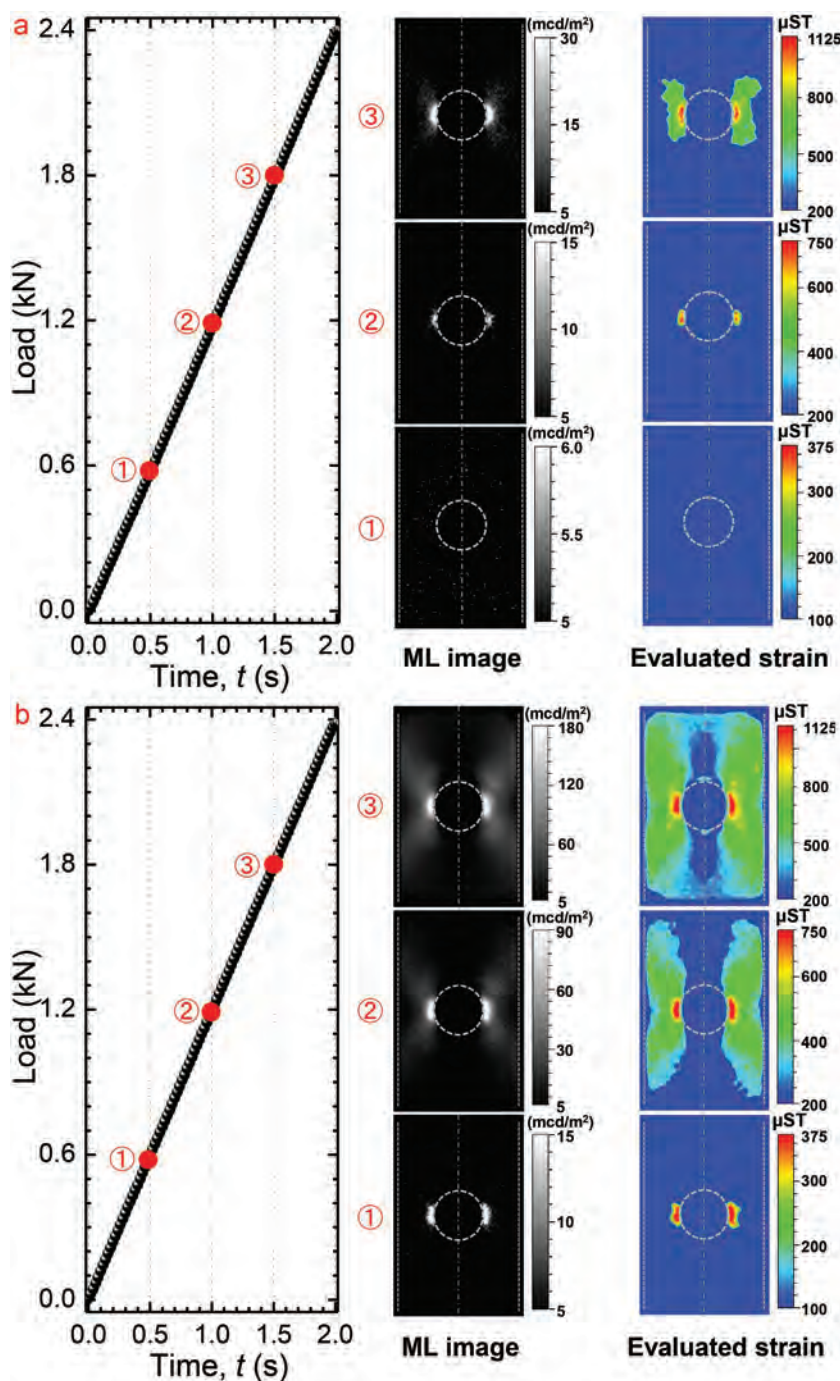
4. Onsite Diagnosis of Large-Scale Infrastructures

4.1. Real-Time Microcrack Imaging

To prevent fracture, real-time microcrack imaging is an important index. The precise image of microcracks, such as length and crack mouth opening displacement (CMOD) of a closed fatigue crack, is difficult to directly observe by conventional strain gauge and also strain/stress sensing methods using

electrical resistance or capacitive MEMS strain sensors and piezoelectric sensors[5–8] because of the discontinuity around the microcrack. However, when an ML paint sensor is bonded over the cracks, the ML sensor is continuous and 2D distribution of cracks and the CMOD can cause stress concentration and generate observable ML on the sensor when mechanical stimulus is applied, and the quantitative images of both ML and evaluated strain would precisely show both the lengths of fatigue-cracks and the strain distribution over the target object. This is another important superiority of ML sensor. As a typical proof test, a 5.0 mm fatigue crack fabricated on a planar stainless steel specimen (JIS SUS430, size of $225 \times 25 \times 3$ mm) is investigated, during which Type 1 and 2 sensors were well painted over the substrate with crack on each side of the specimen. Experimental testing of exactly the same as the previous section was carried out (following the schematic diagram shown in Figure 2a), and only the specimen and loading condition are different. The specimen image and both the experimental and evaluated results are shown in **Figure 5**. Figure 5a shows the photograph and microscopic image of the fatigue crack, and a front view of an ML sensor and a strain gauge on the specimen, where a strain gauge is bonded at about 15 mm far away from the crack and used to control the test machine as a reference strain. The reference strains generated by periodic loads are shown in Figure 5b, during which peak strains of 75 µST were applied to generate clear ML patterns for both Type 1 and 2 sensors although a peak strain of 30 µST can generate enough observable ML for Type 2 sensor. The ML and evaluated strain values for both Type 1 and 2 sensors on the specimen

**ADVANCED
SCIENCE NEWS**

www.advancedsciencenews.com

**ADVANCED
MATERIALS
TECHNOLOGIES**

www.advmattechnol.de

Figure 4. Dynamic imaging of ML and precisely evaluated strains. That for Type 1 a) and Type 2 b) sensors, at times of 0.5, 1.0, and 1.5 s (loads of 0.6, 1.2, and 1.8 kN), respectively.
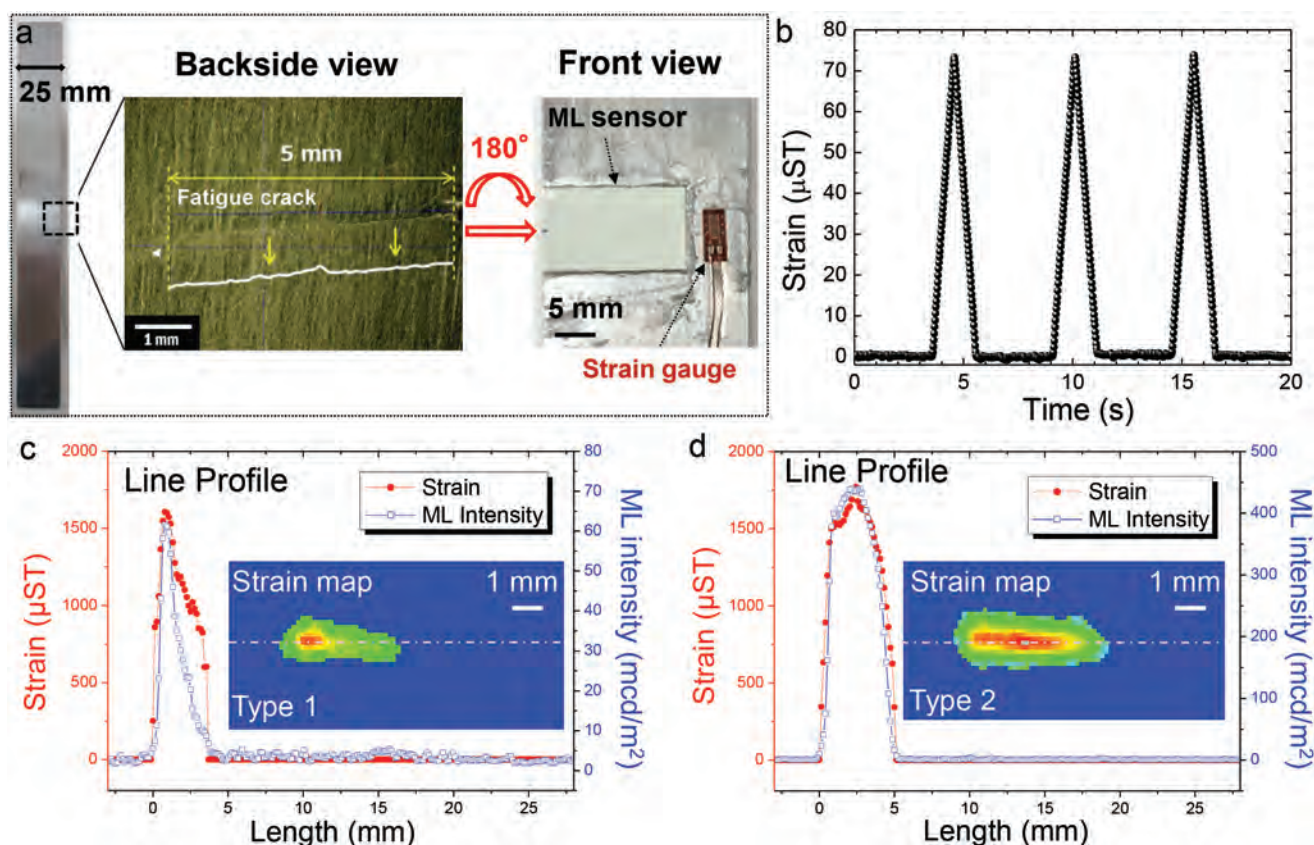
by this novel strain imaging method, and the crack length can be precisely evaluated using Type 2 sensor. It should be noted that a stronger applied strain would further generate stress/strain concentration around the crack tip as similar as the former stress/strain imaging and is not shown here.

4.2. Onsite Large-Scale Infrastructure Diagnosis

The scalable ML sensor is also well applicable for effective diagnosis of fatigue cracks or stress concentration on large-scale infrastructure. The effectiveness in ML measurement has been verified not only by the aforementioned experiments but also on a large-scale infrastructure,[35] however, the strain values are not quantitatively evaluated. Furtherly, comparing to fatigue cracks, another severe infrastructure defect is abnormal stress concentration, which is more difficult to effectively inspect and quantitatively evaluate due to the large-scale and complexity of practical structures. While abnormal stress concentration can easily develop into future fracture or fatigue cracks if not effectively repaired. The ultrasensitive Type 2 sensor can be easily prepared on a large-scale structures and thus especially useful for the effective maintenance oriented preventive measures and lifetime prediction in large-scale, and also of great significance for the quantitative diagnosis of maintenance effectiveness.

To quantitatively evaluate the stress concentration on a large-scale infrastructure, onsite test and dynamic strain imaging were performed on the Urban Expressway (near Kanenokuma Interchange Entrance) in Fukuoka, Japan and a set of results is shown in **Figure 6**. Figure 6a shows an outside image of the inspected infrastructure (urban expressway) as carrying out the field verification test, and Figure 6b shows a future image[50] of onsite inspection when the intersection of a U-rib is inspected.

During the field verification test within steel box girders, Type 2 sensor was well painted on the intersection parts of 12 different U-ribs, where surface cracks on the coatings were observed. A surface crack on the corrosion-proof coating caused by stress concentration does not definitively indicate a fatigue crack on the underneath rib, and in fact the possibility (of a coating surface crack corresponding to a fatigue crack) is less than 1/4 (only 2 determined ones and 1 suspicious one out of 12) during the verification test.[34] Figure 6c–f shows ML and quantitative strain imaging results for a typical stress concentration. Figure 6c,d shows the ML

are shown in Figure 5c,d at the peak load. The strain images in Figure 5c–d show that a maximum strain of 1700–1800 µST was generated on the ML sensors over the crack. Further, based on the line profiles, the crack length is evaluated from Type 2 sensor to be 5.0 mm that is the exact length of the crack owe to the ultra-sensitivity of the sensor, while that evaluated from Type 1 sensor is 3.5 mm. This indicates that the CMOD of a closed fatigue crack can be effectively detected and observed

**ADVANCED
SCIENCE NEWS**
www.advancedsciencenews.com

**ADVANCED
MATERIALS
TECHNOLOGIES**
www.advmattechnol.de

Figure 5. ML measurement and quantitative strain imaging for precise length evaluation of a fatigue crack. a) The photograph and microscopic image of the fatigue crack, and the front view of an ML sensor and a strain gauge bonded on a steel specimen with size of $225 \times 25 \times 3$ mm. b) Absolute strains for reference detected by the strain gauge resulting from periodic loads. ML and evaluated strains on the central line along the length direction of the crack and the pseudo color strain imaging using Type 1 sensor c), and that using Type 2 sensor d).
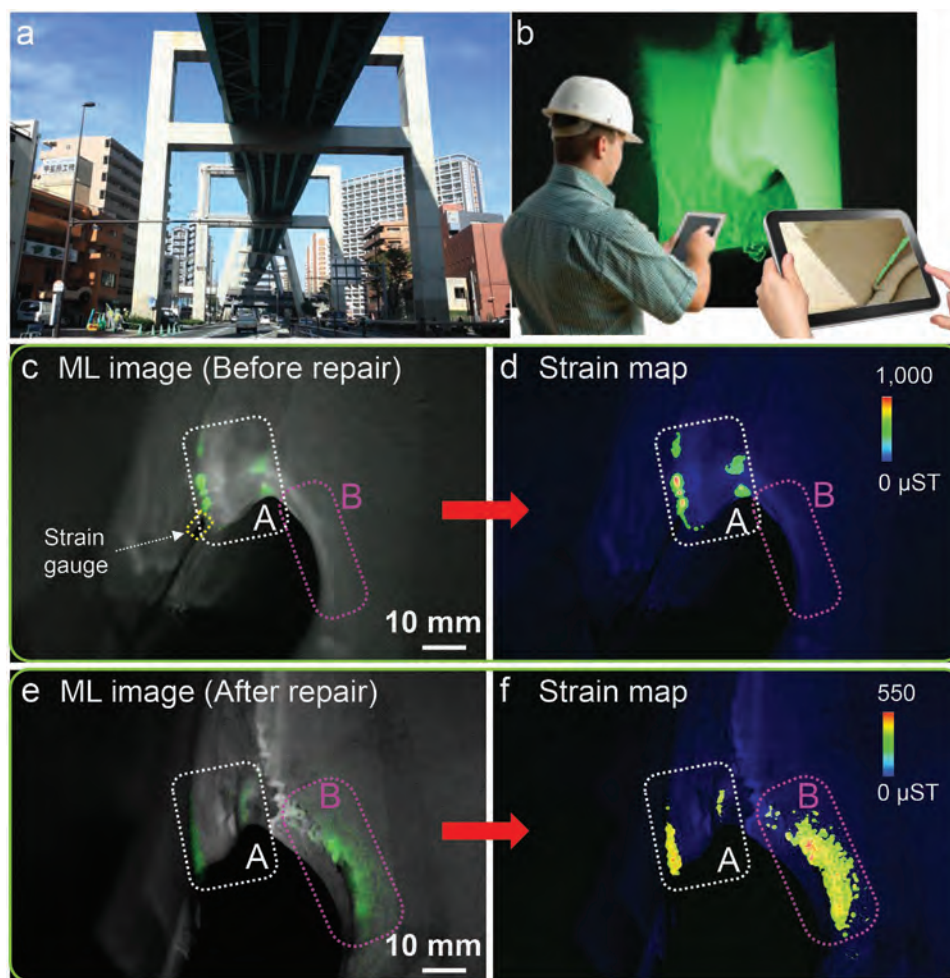
and strain images before the repair work when the peak value of the absolute strain was about 200 µST that was caused by a passing vehicle and detected by the strain gauge enclosed by the dashed yellow line. In this case, the maximum strain at the U-rib was evaluated to be 922 µST, i.e., a value 4.6 times the strain nearby (as shown in the region highlighted by the dotted box A).

In order to diminish the stress concentration, repair work was implemented by grinding the welding section using a grinder, and after the same ML sensor was repainted, the ML and strain images after the repair work are shown in Figure 6e–f. It shows that, after the repair, the maximum strain at the previous "region A" of 4.6 times of stress concentration became 530 µST, which becomes 2.9 times the absolute peak strain nearby (of about 180 µST caused by a passing vehicle). This 40% decrease in stress concentration not only confirms the effectiveness of the repair process but also verifies the effectiveness of this scalable ML sensor on both the quantitative imaging of stress concentration and the unprecedented visible quantitative evaluation of the repair work. The quantitative strain image further reveals that the decrease in stress concentration in "region A" results in spreading of the load of vehicles over a much wider region including "region B" (highlighted by the dotted box B) with a moderate strain value below 500 µST. It further verifies that,

with using this scalable paint sensor, it becomes possible for not only full-field (large-scale) quantitative strain imaging but also effective prediction of the danger region for efficient maintenance, which are the most challenge issues for infrastructural health. Movie S2 in the Supporting Information shows an example of onsite fatigue crack measurement under a similar condition.

It should be noted that, although only the field verification of stress concentration in the intersection part of a U-rib (at a scale of tens of centimeters) was investigated here as an example, the scalable ML sensor is more significantly useful for efficient strain/stress distribution analyses and defect detection in a much large-scale area of meters or tens of meters simply by increasing the sensor painting and camera monitoring area. Movie S3 in the Supporting Information shows an example of larger-scale application on onsite crack monitoring of a concrete bridge. The scalable ML sensor has great significance on more practical infrastructural applications. For real onsite large scale infrastructure diagnosis, the cost issue has also been simulated with the inspection company. As a simulation result, the novel method could be possible to reach more than 80% cost down for crack inspection of high-way bridges, comparing to the conventional method like MT. That is, the novel strain sensors possess great advantage for commercialization and practical worldwide application.

**ADVANCED
SCIENCE NEWS**
www.advancedsciencenews.com

**ADVANCED
MATERIALS
TECHNOLOGIES**
www.advmattechnol.de

Figure 6. Scalable elasticoluminescent sensor for onsite quantitative strain imaging and effective danger-level diagnosis of a highway joint section. a) Outside view of the inspected infrastructure (urban expressway). b) Future image of onsite inspection on infrastructure.[50] Images of ML c) and strain d) show a high stress concentration with a maximum strain of about 1000 µST before repair. Images of ML e) and strain f) show the above concentration with a maximum strain down to about 500 µST after repair (grinding the welding section using a grinder).

5. Conclusion

Precise dynamic stress/strain imaging is critical for a broad range of researches and engineering analyses ranging from micron to meter-scales, and the present work demonstrated the newly-developed scalable elasticoluminescent strain sensor that enables multiscale and precise dynamic strain imaging, during which significant progresses are recently made on both the highly sensitive elasticoluminescent sensors and the quantitative evaluations in dynamic stress/strain imaging. Type 2 sensor has a better sensitivity and Type 1 sensor has a wider applicable strain range, and thus different types of sensors can be optimized for wide range of strain imaging. The precise imaging of stress/strain and the fracture inspection and diagnoses on large-scale infrastructures have been demonstrated. The innovative scalable elasticoluminescent strain sensor would prospectively open a new era in ML and attract wide attentions from the broad array of researchers from material scientists, physicists, chemists, to biologists and structure engineers.

6. Experimental Section

Preparation of Scalable Strain Sensors: The scalable elasticoluminescent sensor for multiscale application is fabricated using ML particles, and the typically used grain sizes are about 1 µm in average as the SEM images shown in Figure 1d,e. Scalable sensor is made of ML paint that consists of ML particles and highly transparent optical epoxy resin. Type 1 and 2 SAOE particles were synthesized by designing a flexible network structure of α-SrAl$_2$O$_4$ using different codoping ions with different sizes, during which a high-purity (>99.9%) ultrafine powder (<0.2 µm) of SrCO$_3$, α-Al$_2$O$_3$ and Eu$_2$O$_3$ with a small amount of codopant ions, calcining in a high vacuum chamber with precise controlling of atmosphere (H$_2$ + Ar).

Type 2 sensor was fabricated by introducing novel codope center of Zr ions in a reduced state, which created new electronic state in the crystal of SAOE and leading to the brighter luminescence especially in small strains. The details of Type 1 and 2 sensors were described in refs. [51] and [52] respectively.

Uniform paint film sensor (as shown in Figure 1e) with a designable uniform thickness is fabricated by screen-printing or spraying the ML paint on a flexible film substrate and the following drying process. This type of scalable strain sensor is flexible and suitable for multiscale 2D planar objects (it can be bonded directly to the surfaces) with

high-precision strain/stress evaluation (e.g., the sensors utilized in Figures 1e and 2–5).

Onsite-dried strain sensor that is fabricated by spraying the ML paint kept beforehand inside a high-pressure bottle onto irregular objects and the following onsite drying process. This type of scalable strain sensor is mostly suitable for application on irregular 3D surfaces (e.g., the sensors used in Figures 1f–g and 6).

Luminance Calibration of Imaging System: In order to measure the absolute luminance in SI unit cd m^{-2} of the ML paint sensor, the imaging system was calibrated to the SI unit. A CCD camera ideally may have a linear characteristic luminance–voltage relationship over a wide luminance range, and the relationship between the luminance, I_{lum}, and the digital intensive value of a pixel in the image, I_{pix}, for digital cameras can be expressed as[53]

$$I_{lum} = I_{pix} \cdot \left[F^2/(tSG) \right] \cdot k_0 \tag{1}$$

where F is the aperture number; t is the exposure time; S is ISO speed or sensor light sensitivity; G is the gain factor, and k_0 is the calibration constant of the camera. When F, S, G, and t are all fixed for a given camera, a much simpler formula can be derived from Equation (1) as follows

$$I_{lum} = k_1 \cdot I_{pix} \tag{2}$$

where k_1 is the total calibration constant of the camera. Thus, for such a given camera system, Equation (2) means that k_1 can be calibrated once and used forever. Moreover, Equations (1) and (2) show that the luminance calibration is independent of the camera-to-subject distance, and this enables effective application to specimens having either smooth surfaces or irregular ones with sags and crests. Based on these, the ML imaging system can be calibrated once and used for all before ML image measurement.

Standard Condition for Quantitative Strain Evaluation: To realize the sensitive, reproducible, and quantitative strain evaluation, the measurement condition was optimized to a standard condition that ML paint sensors were exposed to blue LED (central wavelength: 460–470 nm) for 60 s, and after 300 s, the ML intensity under a load was measured. All the measurements for quantitative strain evaluation are carried out under this standard condition. The aforementioned 60 and 300 s, respectively, are noted as the irradiation and waiting times of the measurement condition. Based on the examination of the standard condition, plenty of irradiation and waiting times are examined. Light irradiation under the standard irradiation time is utilized to reset the ML paint sensor for stably reproducible ML, and the waiting time is standardized for ML measurement under a stable condition with low-level background noise of afterglow intensity. The aforementioned standard condition is robust for a blue LED with a power density of 0.5–2.7 mW cm^{-2} on the paint sensor. The maximum derivation value was confirmed to be ±3.3% when the power density of the irradiation light changed to five-fold stronger, and the robustness and repeatability of the experimental measurement system were confirmed to have the maximum derivation values of the ML peak intensities of ±1.7% under repetitive ML measurements (refer to Figure S1 in the Supporting Information for more detailed information).

Relationship between ML and Strain/Stress (for Quantitative Strain Evaluation): Accurate calculation or calibration of the relationship between the ML and strain is indispensable to precisely evaluate the strain/stress from ML. Figure 2a shows the schematic diagram of the ML measurement system that consists of three parts: 1) a CCD camera (TXG04, Baumer, Radeberg, Germany) with light source for capturing real-time ML images; 2) a mechanical test machine for applying load (MTS 810, MTS Systems Corporation, Eden Prairie, MN USA); 3) a computer that controls the light source and mechanical load with data logger (NR-500, Keyence Co., Osaka, Japan), and records ML images in real-time and records the synchronous strain data through a high-precision strain gauge (KFG-2–120-C1–11L1M2R; Kyowa Electronic Instruments Co., Ltd., Tokyo, Japan). The test piece used in Figure 2

for calibration was a stainless steel specimen (JIS SUS631, size of $200 \times 20 \times 0.5$ mm), and uniform ML paint sensor of Type 1 or 2 SAOE (thickness values of 85.9 and 83.9 μm, respectively) was tightly bonded near the specimen center on each side. The MTS load was controlled using the high-precision strain gauge that was tightly bonded on the specimen. The CCD camera was used for ML image measurement, and small strains of 0–200 μST shown in Figure 2c were detected by a lab-built photon counting system that consists of a photomultiplier tube (PMT, R649, Hamamatsu Photonics, Hamamatsu, Japan) and a photon counter (C5410-51, Hamamatsu Photonics), with a gate time of 10 ms, and controlled to constant strain rate.

Systematic measurements of different maximum strain values and strain loading rates for various types of SAOE sensors through the past 10 years reveal that the relationship between the strain and ML intensity and its variance rate is stable at a specific strain range for each sensor (of a fixed type and thickness). For a given sensor type and thickness, ML intensity depends strongly on both the strain and its variance rate, and vice versa, the strain depends on both ML intensity and its variance rate. Consequently, both ML intensity and its variance rate should be taken into account to enable precise strain evaluation. The relationship between the strain and ML intensity and its variance rate can be expressed as follows (F means the function)

$$\varepsilon = F\left(I, \dot{I}\right) \tag{3a}$$

$$I = I_0 - I_{BG}, \dot{I} = \frac{dI}{dt} = \frac{\Delta I}{\Delta t} \tag{3b}$$

where ε is the strain and has a linear relationship with the applied stress σ of $\varepsilon = \sigma/E$ for elastic deformation (E is the Young's modulus); I and $\dot{I}$ are the value and variance rate of ML intensity (expressed in luminance, i.e., cd/m^2); I_0 is the luminance including both the ML and background afterglow intensities, and I_{BG} is the background intensity that can be precisely measured under the standard condition beforehand or using curve fitting method. It is confirmed that there are generally three undetermined coefficients related the strain to I and $\dot{I}$, and the these coefficients can be calibrated during a pretest using a simple reference specimen (such as a standard planar specimen coated with an ML paint sensor of the same type and thickness as that to be utilized on the target objects).

For effective calibration, ML and synchronous strain values are measured at different strain increasing rates. Since there is a linear relation between the stress and strain under elastic deformation conditions, the evaluated strain or stress has the same precision.

Precise Dynamic Strain Imaging: The test piece used in Figure 3 was an Al alloy plate (JIS A5052, Young's modulus 70.6 GPa, Poisson's ratio 0.33, size of $225 \times 25 \times 2.9$ mm) with a circular hole of 10.7 mm in diameter, and Type 1 or 2 paint sensor was bonded tightly to the central 40×25 mm area on each side. ML images at a maximum load of 2.4 kN and load increasing rate of 1.2 kN s^{-1} were recorded by the CCD camera at 10 FPS, and were compared with the equivalent strains of a pair of (3-axis) rosette strain gauges and the simulated ones by finite element method (FEM; ANSYS Ver. 12.0). The mentioned two strain gauges were bonded around the hole on another Al alloy specimen of the same series as shown in Figure 3b.

Supporting Information

Supporting Information is available from the Wiley Online Library or from the author.

Acknowledgements

[1] C. Li, C. N. Xu, L. Zhang, H. Yamada, Y. Imai, *J. Visualization* **2008**, *11*, 329.

[2] M. Liao, T. Okazaki, R. Ballarini, A. Schultz, T. Galambos, *J. Struct. Eng.* **2011**, *137*, 59.

[3] A. H. Alavi, H. Hasni, N. Lajnef, K. Chatti, F. Faridazar, *Autom. Constr.* **2016**, *62*, 24.

[4] Crack found in Shinkansen trainset bogie. Railway Gazette, http://www.railwaygazette.com/news/high-speed/single-view/view/crack-found-in-shinkansen-trainset-bogie.html (accessed: December 2017).

[5] G. Song, H. Gu, Y.-L. Mo, *Smart Mater. Struct.* **2008**, *17*, 033001.

[6] A. A. Mohammed, W. A. Moussa, E. Lou, *Sensors* **2008**, *8*, 2642.

[7] K. Singh, R. Joyce, S. Varghese, J. Akhtar, *Sens. Actuators, A* **2015**, *223*, 151.

[8] S. G. Rauscher, H. A. Bruck, D. L. DeVoe, *Sens. Actuators, A* **2018**, *269*, 474.

[9] S. A. Mascaro, H. H. Asada, *IEEE Trans. Rob. Autom.* **2001**, *17*, 698.

[10] F. Patolsky, B. P. Timko, G. Yu, Y. Fang, A. B. Greytak, G. Zheng, C. M. Lieber, *Science* **2006**, *313*, 1100.

[11] J. J. Boland, *Nat. Mater.* **2010**, *9*, 790.

[12] D. H. Kim, N. Lu, R. Ma, Y. S. Kim, R. H. Kim, S. Wang, J. Wu, S. M. Won, H. Tao, A. Islam, K. J. Yu, T. I. Kim, R. Chowdhury, M. Ying, L. Xu, M. Li, H. J. Chung, H. Keum, M. McCormick, P. Liu, Y. W. Zhang, F. G. Omenetto, Y. Huang, T. Coleman, J. A. Rogers, *Science* **2011**, *333*, 838.

[13] K. Takei, T. Takahashi, J. C. Ho, H. Ko, A. G. Gillies, P. W. Leu, R. S. Fearing, A. Javey, *Nat. Mater.* **2010**, *9*, 821.

[14] S. C. B. Mannsfeld, B. C-K. Tee, R. M. Stoltenberg, C. V. H. Chen, S. Barman, B. V. O. Muir, A. N. Sokolov, C. Reese, Z. Bao, *Nat. Mater.* **2010**, *9*, 859.

[15] D. J. Lipomi, M. Vosgueritchian, B. C.-K. Tee, S. L. Hellstrom, J. A. Lee, C. H. Fox, Z. Bao, *Nat. Nanotechnol.* **2011**, *6*, 788.

[16] D. Cho, J. Park, J. Kim, T. Kim, J. Kim, I. Park, S. Jeon, *ACS Appl. Mater. Interfaces* **2017**, *9*, 17369.

[17] C. Pan, L. Dong, G. Zhu, S. Niu, R. Yu, Q. Yang, Y. Liu, Z. L. Wang, *Nat. Photonics* **2013**, *7*, 752.

[18] X. Wang, M. Que, M. Chen, X. Han, X. Li, C. Pan, Z. L. Wang, *Adv. Mater.* **2017**, *29*, 1605817.

[19] D. Son, J. Lee, S. Qiao, R. Ghaffari, J. Kim, J. E. Lee, C. Song, S. J. Kim, D. J. Lee, S. W. Jun, S. Yang, M. Park, J. Shin, K. Do, M. Lee, K. Kang, C. S. Hwang, N. Lu, T. Hyeon, D. H. Kim, *Nat. Nanotechnol.* **2014**, *9*, 397.

[20] D. Kang, P. V. Pikhitsa, Y. W. Choi, C. Lee, S. S. Shin, L. Piao, B. Park, K. Y. Suh, T. I. Kim, M. Choi, *Nature* **2014**, *516*, 222.

[21] B. Park, J. Kim, D. Kang, C. Jeong, K. S. Kim, J. U. Kim, P. J. Yoo, T.-I. Kim, *Adv. Mater.* **2016**, *28*, 8130.

[22] Y. Y. Hui, X. Liu, W. Jie, N. Y. Chan, J. Hao, Y.-T. Hsu, L.-J. Li, W. Guo, S. P. Lau, *ACS Nano* **2013**, *7*, 7126.

[23] Y. Chen, Y. Zhang, D. Karnaushenko, L. Chen, J. Hao, F. Ding, O. G. Schmidt, *Adv. Mater.* **2017**, *29*, 1605165.

[24] C. N. Xu, T. Watanabe, M. Akiyama, X. G. Zheng, *Appl. Phys. Lett.* **1999**, *74*, 1236.

[25] C. N. Xu, T. Watanabe, M. Akiyama, X. G. Zheng, *Appl. Phys. Lett.* **1999**, *74*, 2414.

[26] C. N. Xu, X. G. Zheng, M. Akiyama, K. Nonaka, T. Watanabe, *Appl. Phys. Lett.* **2000**, *76*, 179.

[27] C. N. Xu, *Encyclopedia of Smart Material*, Vol. *1*, John Wiley & Sons, Inc., NY **2002**, p. 190.

[28] C. N. Xu, H. Yamada, X. Wang, X. G. Zheng, *Appl. Phys. Lett.* **2004**, *84*, 3040.

[29] X. S. Wang, C. N. Xu, H. Yamada, K. Nishikubo, X. G. Zheng, *Adv. Mater.* **2005**, *17*, 1254.

[30] C. Li, C. N. Xu, Y. Imai, N. Bu, *Strain* **2011**, *47*, 483.

[31] C. N. Xu, *Proc. Intl. Forum Mechanoluminescence Novel Structural Health Diagnosis* **2011**, 6.

[32] K. Hyodo, C. N. Xu, H. Mishima, S. Miyakawa, *Proc. Intl. Forum Mechanoluminescence Novel Structural Health Diagnosis* **2011**, 61.

[33] N. Terasaki, C. N. Xu, *IEEE Sens. J.* **2013**, *13*, 3999.

[34] Y. Fujio, C. N. Xu, Y. Terasawa, Y. Sakata, J. Yamabe, N. Ueno, N. Terasaki, A. Yoshida, S. Watanabe, Y. Murakami, *Int. J. Hydrogen Energy* **2016**, *41*, 1333.

[35] A. Yoshida, L. Liu, D. Tu, S. Kainuma, C. N. Xu, *J. Disaster Res.* **2017**, *12*, 506.

[36] J. S. Kim, K. Kibble, Y. N. Kwon, K. S. Sohn, *Opt. Lett.* **2009**, *34*, 1915.

[37] S. M. Jeong, S. Song, S.-K. Lee, B. Choi, *Appl. Phys. Lett.* **2013**, *102*, 051110.

[38] G. J. Yun, M. R. Rahimi, A. H. Gandomi, G. C. Lim, J. S. Choi, *Smart Mater. Struct.* **2013**, *22*, 055006.

[39] S. Someya, K. Ishii, T. Munakata, M. Saeki, *Opt. Express* **2014**, *22*, 21991.

[40] M. R. Rahimi, G. J. Yun, J.-S. Choi, *Acta Mater.* **2014**, *77*, 200.

[41] C. N. Xu, *Hyomen Kagaku* **2008**, *29*, 229 (in Japanese).

[42] C. Li, Y. Imai, Y. Adachi, H. Yamada, K. Nishikubo, C. N. Xu, *J. Am. Ceram. Soc.* **2007**, *90*, 2273.

[43] H. Yamada, C. N. Xu, *J. Appl. Phys.* **2007**, *102*, 126103.

[44] H. Matsuo, K. Ikeda, S. Hata, H. Nakashima, H. Yamada, C. N. Xu, *J. Alloys Compd.* **2013**, *577*, S507.

[45] M. Kawai, M. Futakawa, T. Naoe, H. Yamada, C. N. Xu, *Eng. Trans.* **2011**, *59*, 13.

[46] X. Wang, H. Zhang, R. Yu, L. Dong, D. Peng, A. Zhang, Y. Zhang, H. Liu, C. Pan, Z. L. Wang, *Adv. Mater.* **2015**, *27*, 2324.

[47] X. Wang, R. Ling, Y. Zhang, M. Que, Y. Peng, C. Pan, *Nano Research.* **2018**, *11*, 1967.

[48] D. Tu, C. N. Xu, A. Yoshida, M. Fujihala, J. Hirotsu, X. G. Zheng, *Adv. Mater.* **2017**, *29*, 1606914.

[49] X. Liu, K. Kim, Y. Zhang, Y. Sun, *Int. J. Rob. Res.* **2009**, *28*, 1065.

[50] C. N. Xu, *SIP, Infrastructure Maintenance, Renovation and Management*, https://www.jst.go.jp/sip/dl/k07/booklet_en/36.pdf (accessed: March 2017).

[51] C. N. Xu, *US8,128,839B2*, **2012**.

[52] C. N. Xu, D. Tu, *WOPI/PCT, WO 2018/135106*, **2018**.

[53] a) F. Vesali, M. Omid, A. Kaleita, H. Mobli, *Comput. Electron. Agricult.* **2015**, *116*, 211; b) P. D. Hiscocks, *Syscomp Electronic Design Limited*, https://atecorp.com/atecorp/media/pdfs/data-sheets/Tektronix-J16_Application.pdf (accessed: September 2011).